

11th U.S. National Combustion Meeting
Organized by the Western States Section of the Combustion Institute
March 24–27, 2019
Pasadena, California

Direct numerical simulation of high-pressure mixing in turbulent jets

*Nek Sharan*¹ and *Josette Bellan*^{1,2,*}

¹*Mechanical and Civil Engineering, California Institute of Technology, Pasadena, CA 91125, USA*

²*Jet Propulsion Laboratory, California Institute of Technology, Pasadena, CA 91109, USA*

**Corresponding author: josette.bellan@jpl.nasa.gov*

Abstract: Combustion in automotive and aerospace applications employing diesel, gas turbine and liquid rocket engines is preceded by injection and mixing of fuel and oxidizer at high pressures, often exceeding mixture critical values. Experimental observations indicate that the jets injected at supercritical pressures exhibit significantly different dynamics than the jets at subcritical conditions, owing to the lack of distinct liquid and gas phases in supercritical state. As a result, the averaged flow quantities such as the potential core length, jet spatial growth rate and velocity decay profiles differ in the two conditions, resulting in different mixed-fluid distributions. In this study, turbulent jet direct numerical simulations (DNS) are performed to examine the variations in statistics between injection of Nitrogen (N₂) in Nitrogen (N₂) at subcritical (perfect-gas) and supercritical conditions. Isothermal round jets at Reynolds number (Re_D), based on jet diameter (D) and jet orifice velocity (U_0), of 5000 and Mach number of 0.6 are considered. For mixing analyses, a passive scalar transported with the flow is examined.

Keywords: *Injection, Mixing, Turbulence, Supercritical conditions*

1. Introduction

Fuel injection and turbulent mixing at supercritical pressures determines ignition and combustion in numerous engineering applications. Flow evolution under such conditions is characterized by strong non-linear coupling between dynamics, transport coefficients, and thermodynamics. A model that accounts for these non-linear effects in computation of the thermodynamic state of the mixture, and the heat and mass fluxes in a multi-component fluid-flow simulation was proposed by Masi *et al.* [1]. The goal of the present study is to evaluate the model in a turbulent free-jet configuration to simulate fuel injection and mixing in high-pressure(p) combustion chambers of propulsion systems.

Validation of numerical simulations at high- p conditions, where theoretical results are scarce, requires comparisons with experimental data. However, most experimental studies (*e.g.*, [2–4]) inject liquid (fuel at subcritical conditions) or high-density fluid (fuel at supercritical conditions) at high Reynolds numbers ($Re_D \geq 20,000$), and provide qualitative visual information about flow dynamics and mixing. A numerical simulation of these flows, for direct comparisons with the experiments, would require several models. For example, models to accommodate potential two-phase/density-jump regions and to account for the subgrid-scale fluxes would be required, in addition to the thermodynamic model. Moreover, appropriate inflow and boundary treatments that

accurately replicate the experimental conditions are also imperative. Interactions between the models and numerical details make validation of individual models infeasible in such complex flows at high- Re_D . Moreover, the lack of quantitative turbulence/mixing statistics measurements in high- p experiments makes assessment of a model even more challenging.

To mitigate the model interactions, direct numerical simulations at Re_D of 5,000 are considered in this study. Jet flow at perfect-gas conditions, for which theoretical [5, 6] and experimental [7, 8] results exist, is first considered to validate the numerical setup and to create a database for flow-behavior comparisons against multicomponent flows at high pressures. To systematically initiate the study, mixing behavior in the single-species flows is assessed by a virtual passive scalar transported with the flow, modeling diffusion at unity Schmidt number (Sc) justifiable under perfect-gas conditions.

Accurate turbulent free-jet flow computation requires a careful choice of inflow/boundary conditions, domain size, and numerical discretization. The near-field jet flow evolution is particularly sensitive to the choice of inflow perturbations, and several studies [9, 10] have examined its influence on turbulence statistics. The jet flow attains self-similarity after the development region, containing potential core collapse and transition to turbulence; the axial distance to attain a self-similar state depends on the inflow perturbations. Moreover, theoretical results [11] suggest that the self-similar state may also depend on the inflow, requiring the similarity variables to be appropriately modified for analyses. Although the theoretical and experimental jet flow studies focus on the flow statistics in the self-similar region, in practical applications with small combustion chambers, the jet near-field is equally important because this is where the phenomena determining the flame occur, and this is where control must be exercised to influence flow behavior.

2. Governing equations

For the single-species flow of interest here, the conservation equations solved in this study are:

$$\frac{\partial \rho}{\partial t} + \frac{\partial}{\partial x_j} [\rho u_j] = 0, \quad (1)$$

$$\frac{\partial}{\partial t} (\rho u_i) + \frac{\partial}{\partial x_j} [\rho u_i u_j + p \delta_{ij} - \sigma_{ij}] = 0, \quad (2)$$

$$\frac{\partial}{\partial t} (\rho e_t) + \frac{\partial}{\partial x_j} [(\rho e_t + p) u_j - u_i \sigma_{ij} + q_j] = 0, \quad (3)$$

$$\frac{\partial}{\partial t} (\rho \xi) + \frac{\partial}{\partial x_j} [\rho \xi u_j + J_j] = 0, \quad (4)$$

where t denotes the time, x is a Cartesian coordinate, subscripts i and j refer to the spatial coordinates, u_i is the velocity, p is the pressure, δ_{ij} is the Kronecker delta, $e_t = e + u_i u_i / 2$ is the total energy (*i.e.*, internal energy, e , plus kinetic energy), $\xi \in [0, 1]$ is a virtual passive scalar transported with the flow, σ_{ij} is the Newtonian viscous stress tensor

$$\sigma_{ij} = \mu \left(2S_{ij} - \frac{2}{3} S_{kk} \delta_{ij} \right), \quad S_{ij} = \frac{1}{2} \left(\frac{\partial u_i}{\partial x_j} + \frac{\partial u_j}{\partial x_i} \right), \quad (5)$$

where μ is the viscosity, S_{ij} is the strain-rate tensor, and $q_j = -\lambda \partial T / \partial x_j$ and $J_j = -\mathcal{D} \partial \xi / \partial x_j$ are the j -direction heat flux and scalar diffusion flux, respectively. λ is the thermal conductivity and $\mathcal{D} = \mu / Sc$ is the scalar diffusivity, where Sc denotes the Schmidt number. The injected fluid is assigned a scalar value of 1, whereas the chamber fluid a value of 0.

Two jet-flow simulations at conditions summarized in Table 1 are performed to examine flow statistics differences between injection at perfect-gas and supercritical conditions. Only the chamber pressure p_∞ differs between the two cases.

For the near-atmospheric- p simulation (Case 1), the perfect gas equation of state is applicable, given by

$$p = \frac{\rho R_u T}{m},$$

where R_u is the universal gas constant and m is the species molar mass. The viscosity is modeled as a power law

$$\mu = \mu_R \left(\frac{T}{T_R} \right)^n$$

with $n = 2/3$ and the reference viscosity $\mu_R = \rho_0 U_0 D / Re_D$, where ρ_0 and U_0 are the jet-exit fluid density and velocity, respectively, and the reference temperature $T_R = 293$ K. The thermal conductivity $\lambda = \mu C_p / Pr$, where Prandtl number $Pr = 0.7$, the ratio of specific heats $\gamma = 1.4$, and the isobaric heat capacity $C_p = \gamma R_u / (\gamma - 1)$ is assumed.

For the high- p simulation (Case 2), the governing equations (1)-(4) are closed using the Peng-Robinson (PR) equation of state (EOS)

$$p = \frac{R_u T}{(v_{PR} - b_{mix})} - \frac{a_{mix}}{(v_{PR}^2 + 2b_{mix}v_{PR} - b_{mix}^2)},$$

where the pressure, p , and temperature, T , are obtained as an iterative solution from the density, ρ , and internal energy, e , obtained from the conservation equations [12]. The molar PR volume $v_{PR} = v - v_s$, where the molar volume $v = m / \rho$. v_s denotes the volume shift introduced to improve the accuracy of the PR EOS at high pressures [12, 13]. a_{mix} and b_{mix} are obtained from the expressions detailed in [14, Appendix B].

The physical viscosity, μ_{ph} , and thermal conductivity, λ_{ph} , are calculated using the Lucas method [15, Chapter 9] and the Stiel-Thodos method [15, Chapter 10], respectively. The computational viscosity, μ , and thermal conductivity, λ , are then obtained by scaling μ_{ph} and λ_{ph} with factor $\mathcal{F} = \mu_R / \mu_{ph,0}$, *i.e.*, $\mu = \mathcal{F} \mu_{ph}$ and $\lambda = \mathcal{F} \lambda_{ph}$, to simulate the flow at a specified Reynolds number Re_D . The inflow physical viscosity, $\mu_{ph,0}$, is obtained from the Lucas method using the pressure p_∞ and the average temperature $(T_{inj} + T_{ch}) / 2$, where the subscripts ‘‘inj’’ and ‘‘ch’’ denote the injection and chamber conditions, respectively.

To examine the robustness of the above EOS and transport coefficient models at supercritical conditions, Figure 1 compares the density, isobaric heat capacity, and the transport coefficients μ_{ph} and λ_{ph} obtained from the models against the National Institute of Standards and Technology (NIST) database [16] for N_2 at a pressure of 50 bar and temperatures ranging from 100 K to 400 K. The supercritical temperature (T_c) of Nitrogen is 126.2 K. The transport coefficient models are accurate only at supercritical temperatures and, thus, the comparison only spans values of $T > T_c$. As evident, the models have good agreement with the NIST database, showing their validity at high- p conditions encountered during Case 2 simulation. Figure 2 shows the compressibility factor

(Z), indicating deviation from perfect-gas behavior, of pure Nitrogen for a temperature range at 50 bar pressure. The compressibility factor at chamber conditions in Case 2 is 0.994.

Case	$N_x \times N_y \times N_z$	p_∞ (bar)	T_{ch} (K)	T_{inj} (K)	Number of species	Re_D	Ma_0	Inflow velocity perturbation amplitude
1 (atmP)	$320 \times 288 \times 288$	1	293	293	1 (N_2)	5000	0.6	$0.004U_0$
2 (highP)	$320 \times 288 \times 288$	50	293	293	1 (N_2)	5000	0.6	$0.004U_0$

Table 1: Summary of the conditions for the numerical simulations.

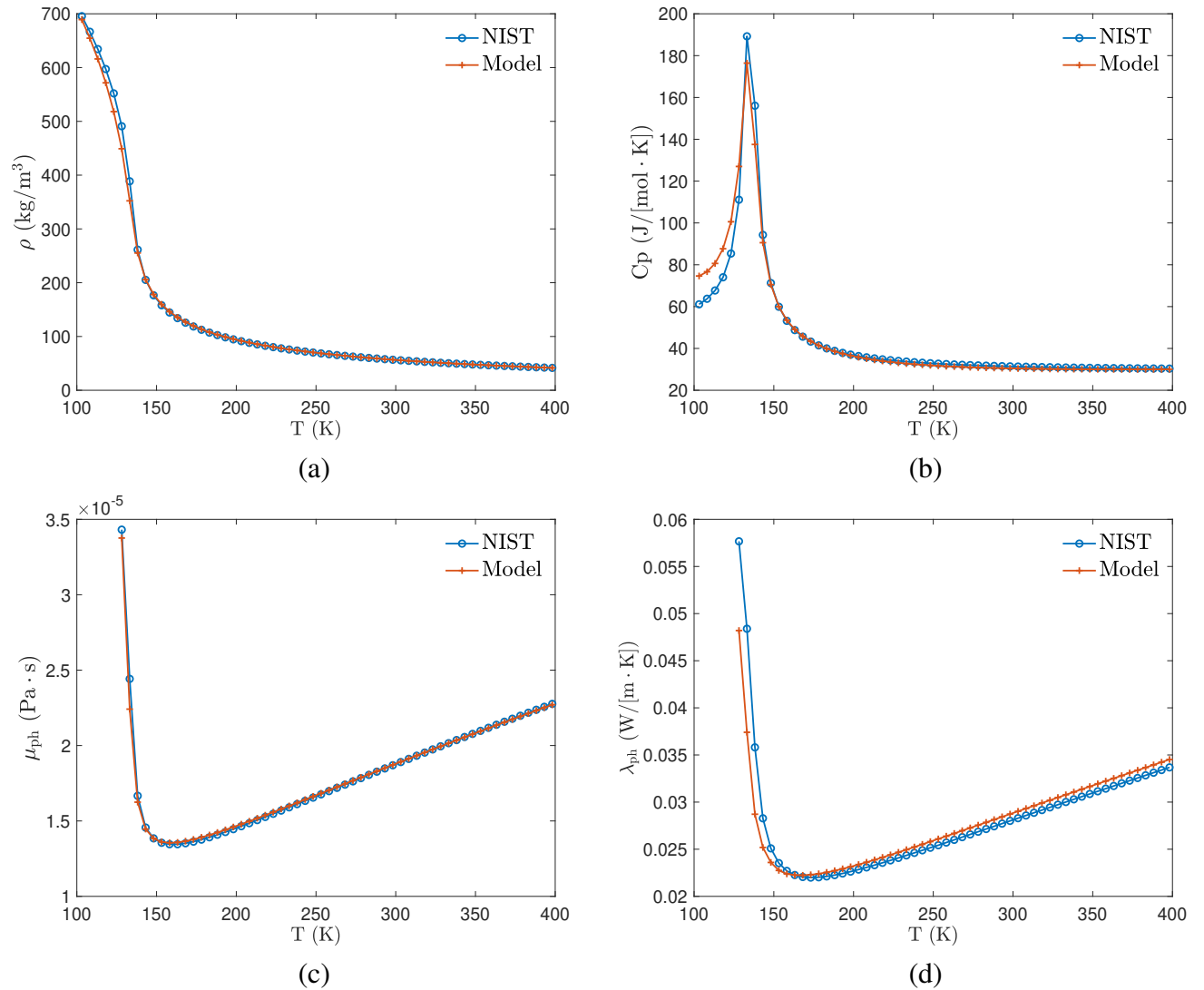


Figure 1: EOS and transport coefficients model comparison against NIST database for pure Nitrogen at 50 bar pressure. (a) Density, (b) Isobaric heat capacity, (c) Viscosity, and (d) Thermal conductivity.

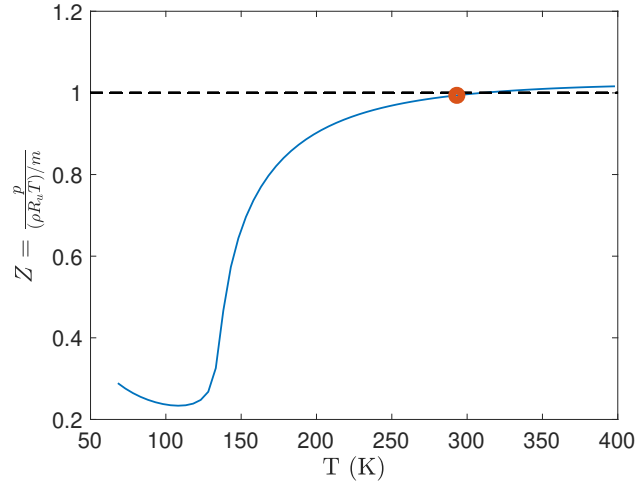


Figure 2: Compressibility factor of N_2 at 50 bar pressure. Red marker denotes the chamber conditions for Case 2.

3. Numerical details

The spatial derivatives are approximated using the sixth-order compact finite-difference scheme and time integration uses the explicit fourth-order Runge-Kutta method. The outflow boundary in axial direction and all lateral boundaries have sponge zones[17] with subsonic non-reflecting outflow Navier-Stokes characteristic boundary conditions (NSCBC)[18] at the boundary faces. Sponge zones at each outflow boundary have a width of 10% of the domain length normal to the boundary face. The sponge strength at each boundary decreases quadratically with distance normal to the boundary. The performance of one-dimensional NSCBC[18] as well as its three-dimensional extension[19] by inclusion of transverse terms were also evaluated without the sponge zones; they permit occasional spurious reflections into the domain, therefore, the use of sponge zones was deemed necessary. To avoid unphysical accumulation of energy at the highest wavenumber, resulting from the non-dissipative spatial discretization, the conservative variables are filtered every five time steps using an eighth-order filter.

The computational domain extends to $42D_0$ in the axial (x -)direction and $20D_0$ in the y - and z -direction including the sponge zones, as shown in Figure 3. $320 \times 288 \times 288$ grid points are used in the $x \times y \times z$ direction, which is twice the number of grid points in each direction used for DNS by Boersma[20] at similar conditions as Case 1.

The axial grid resolution is chosen to resolve all spatial scales overwhelmingly responsible for the dissipation. Following the approach outlined in [21], for a $Re_D = 5000$ jet simulation, the Kolmogorov length scale $\eta_K = 0.0041(x - x_0)$, where x_0 denotes the virtual origin. A stretched grid designed accordingly is used for present simulations. Grid stretching is accounted for by solving the governing equations in generalized coordinates [22, 23].

The velocity profile at the jet inflow plane is given by[6]

$$u(r) = \frac{U_0}{2} \left(1 - \tanh \left[\frac{r - r_0}{2\theta_0} \right] \right),$$

where the jet exit radius $r_0 = D/2$ and the momentum thickness $\theta_0 = 0.04r_0$ is assumed. The

Mach number $Ma_0 = U_0/c_\infty = 0.6$ is specified, where c_∞ denotes the speed of sound at ambient conditions. Random perturbations with maximum amplitudes of $0.004U_0$ are superimposed on the inflow velocity profile to trigger jet flow transition to turbulence. No perturbations are added to fields other than velocity.

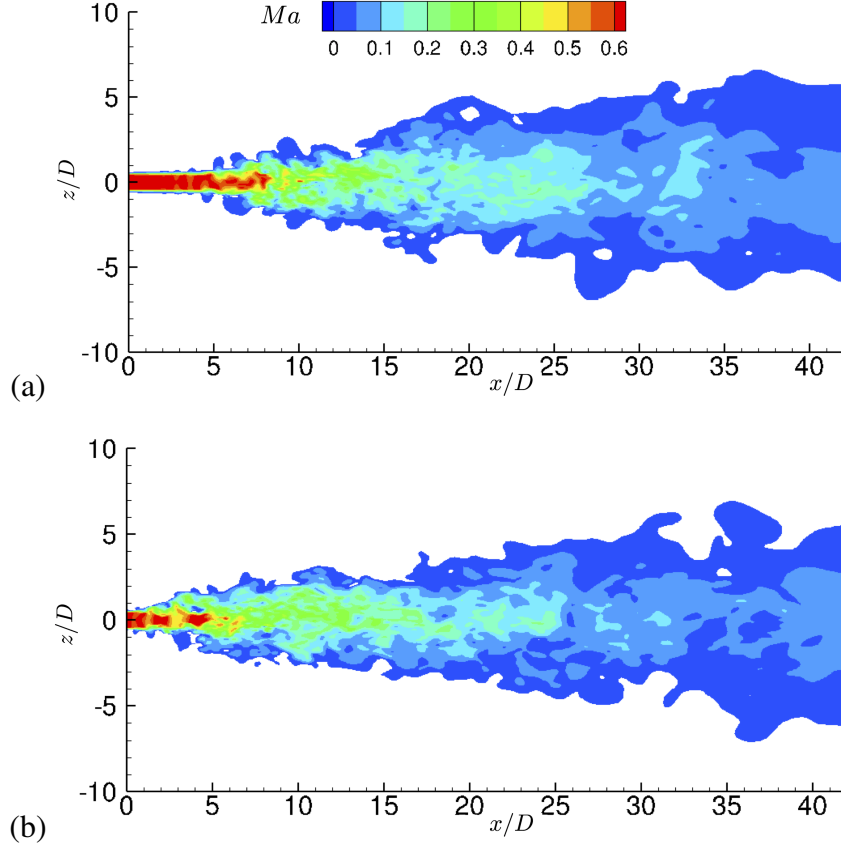


Figure 3: Instantaneous Mach number (Ma) field at $tU_0/D \approx 2500$ in (a) Case 1 and (b) Case 2. Only values of $Ma \geq 0.01$ are rendered. Legend is the same for both plots.

4. Jet flow results and discussion

Table 1 summarizes the conditions for the numerical simulations considered in this study. In both cases, the injected and chamber fluid temperatures and pressures are the same, therefore, the jet injects into a chamber that is as dense as the injected fluid. In other words, Case 1 and 2 represent jets at same temperature and exit velocity, but in Case 1 a near-atmospheric pressure jet is injected into similar chamber conditions and in Case 2 a 50 bar pressure jet is injected into similar chamber conditions. Physically, if the former jet has a Re_D of 5000, the latter jet, based on the density and viscosity at 50 bar pressure and same exit velocity U_0 and diameter D as the velocity and length scale, will have $Re_D \sim 240,000$. A DNS at such Re_D is infeasible, therefore, in this study Re_D is fixed to 5000 for both cases; the $Re_D = 5000$ condition is enforced using a computational viscosity μ that is calculated by scaling the physical viscosity by a factor \mathcal{F} , as discussed in Section 2.

$\mathcal{F} \approx 6.5$ ($\mu_R = \rho_0 U_0 D / Re_D = 1.136 \times 10^{-4}$ Pa.s and $\mu_{ph,0} = 1.757 \times 10^{-5}$ Pa.s) for Case 1, near atmospheric pressure, and $\mathcal{F} \approx 309.4$ ($\mu_R = 5.715 \times 10^{-3}$ Pa.s and $\mu_{ph,0} = 1.847 \times 10^{-5}$ Pa.s)

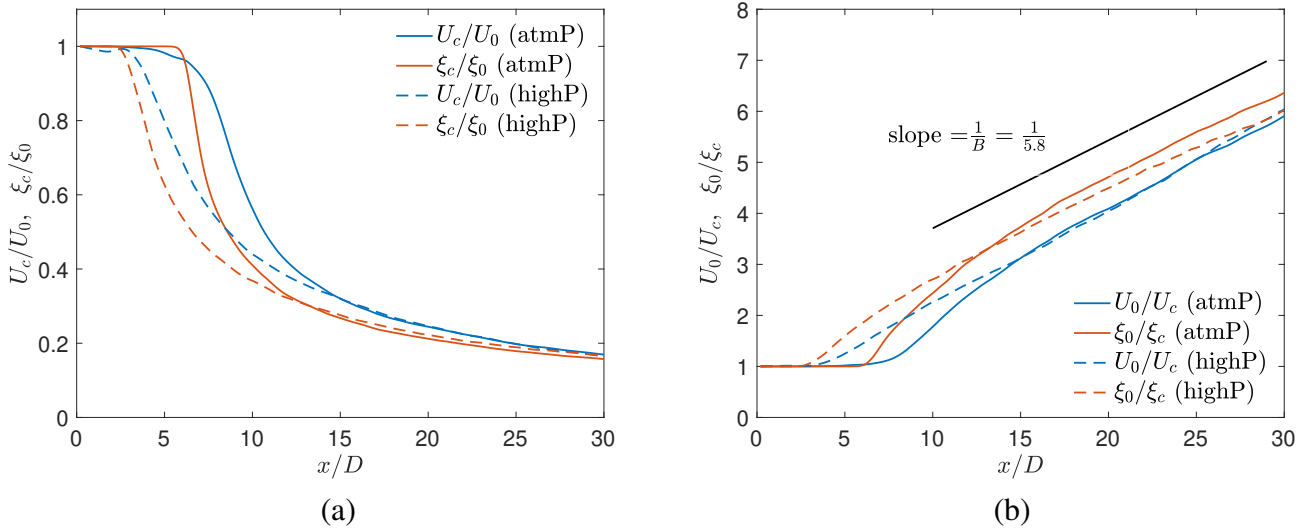


Figure 4: Case 1 and 2 comparison showing (a) the time-averaged centerline velocity (U_c) and scalar (ξ_c) values normalized with the jet exit values U_0 and ξ_0 as a function of axial distance and (b) the inverse of the time-averaged centerline values showing linear decay asymptotically with axial distance.

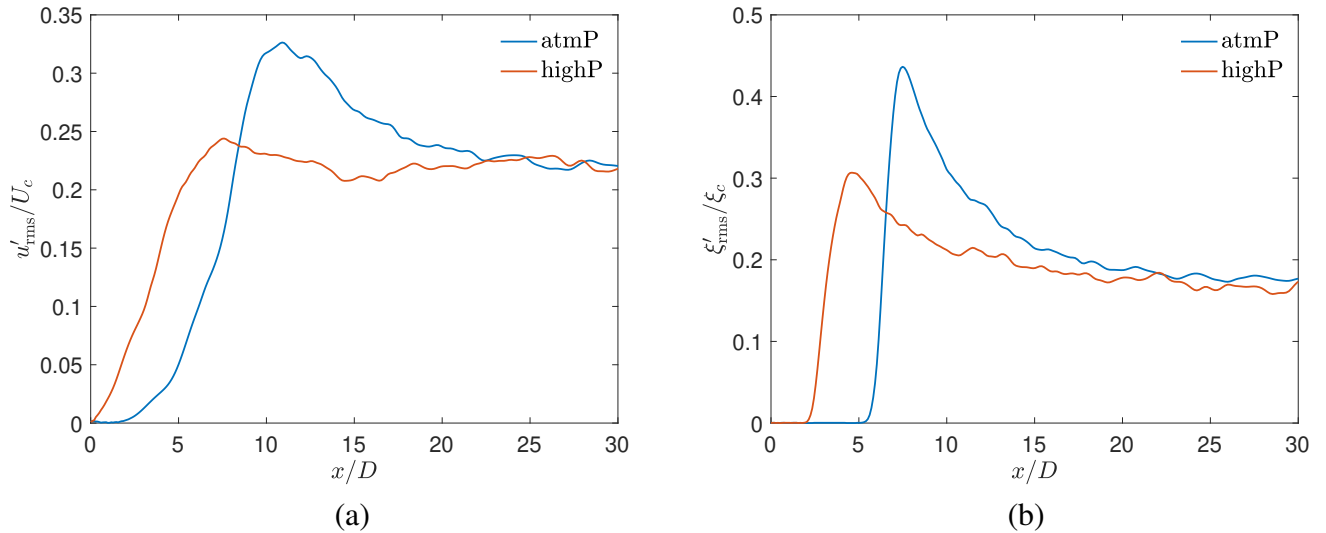


Figure 5: Centerline root-mean-square (a) axial velocity and (b) scalar fluctuation comparison between Case 1 and 2.

for Case 2 at 50 bar pressure. The factor \mathcal{F} is higher in Case 2 because of the higher density ρ_0 at 50 bar that requires a higher μ_R for a given Reynolds number Re_D . The physical viscosity $\mu_{ph,0}$, on the other hand, remains relatively unchanged with increase in pressure. Simulating the two jets at same Reynolds number by using a computational viscosity, as explained above, results in the high- p jet becoming unphysically more viscous than the atmospheric- p jet. The following comparisons between the two cases must account for this effect.

Figure 3 shows the Mach number contours at $tU_0/D \approx 2500$ for both cases. The potential core is comparatively shorter in the high- p case, likely due to higher computational viscosity μ , from a higher value of factor \mathcal{F} , and resulting momentum diffusion.

Figure 4 shows the decay of time-averaged centerline velocity (U_c) and scalar concentration (ξ_c) with axial distance. For a self-similar round jet with top-hat exit velocity profile, the centerline velocity $U_c(x)$ is given by the empirical relation[8]

$$\frac{U_c(x)}{U_0} = \frac{B}{(x-x_0)/D}, \quad (6)$$

where B is a constant and x_0 denotes the virtual origin. As evident from Figure 4(b), downstream of the potential core collapse, both the time-averaged centerline velocity and scalar concentration decays as inverse of the axial distance, where the rate of decay, given by B , is within experimentally observed range of values [8]. The scalar concentration begins to decay upstream of velocity, consistent with the observation of Lubbers *et al.* [24, see Figure 6] for a passive scalar diffusing at unity Schmidt number. Despite the difference in axial location where the velocity or scalar decay begins between the near-atmospheric- p and high- p cases, the profiles match asymptotically with axial distance. At the time of reporting, the scalar statistics for the high- p case did not fully converge; we expect the dashed red line in Figure 4 to asymptotically converge to the solid red line (like the velocity field shown in blue).

Figure 5 shows the centerline root-mean-square (r.m.s.) axial velocity and scalar concentration fluctuation, denoted by u'_{rms} and ξ'_{rms} , respectively, normalized by the time-averaged centerline values. The centerline r.m.s. values are calculated from

$$u'_{\text{rms}} = \left(\overline{(u - U_c)^2} \right)^{1/2} = \left(\overline{u^2} - U_c^2 \right)^{1/2}$$

and a similar expression for scalar concentration. The overbar, $\overline{\bullet}$, denotes a time average at the centerline. The r.m.s. velocity fluctuation profiles in Figure 5(a) compare favorably with the profile of Crow & Champagne [25, see Figure 13] and, similarly, the scalar fluctuation profiles in Figure 5(b) compare well with the distributions of r.m.s. scalar fluctuation in jets from smooth contraction nozzle shown in Mi *et al.* [26, see Figure 4(a)]. As observed in Figure 4, despite the differences in r.m.s. fluctuations in near-jet regions between the high- p and near-atmospheric- p cases, the profiles match asymptotically with axial distance. The fluctuation magnitude signifies turbulence intensity, which is negligible in the potential core, increases sharply with collapse of the core, and asymptotes downstream to a constant value as the flow becomes self-similar. The rise in fluctuation profiles at shorter axial distance in case of high-pressure jet shows a shorter potential core. Relatively lower peak fluctuation amplitudes in high pressure results is likely a manifestation of the higher computational diffusivity from higher value of μ .

5. Conclusions

Single-species turbulent jet simulations at different chamber conditions are performed as part of an effort to understand fuel injection and fuel-oxidizer mixing at high pressures. Two cases with near-atmospheric and supercritical chamber pressures, respectively, are analyzed while keeping inflow, boundary conditions and initial condition identical. The equation of state and transport coefficient

models are chosen specific to the two conditions. The transport property models at supercritical conditions are validated against the NIST database values. To avoid subgrid-scale model errors and its, often difficult to predict, interactions with thermodynamic calculations in high-Reynolds-number simulations, DNS at Re_D of 5000 is performed. Profiles of centerline velocity and scalar concentration mean and r.m.s. fluctuations show favorable agreement with the experimental data at atmospheric- p conditions. For comparisons in this study, the near-atmospheric- p and high- p jets were simulated at the same Reynolds number by using a computational viscosity adjusted accordingly. Matching the Reynolds number in such a manner results in the high- p jet becoming more viscous than the atmospheric- p jet, thus, obscuring mixing statistics' one-to-one comparisons. An alternative is to match the inflow momentum instead of the Reynolds number Re_D , keeping the viscosity physical. This alternative will be a subject of future investigation.

6. Acknowledgements

This work was supported by the Army Research Office under the direction of Dr. Ralph Anthenien. The computational resources were provided by the NASA Advanced Supercomputing at Ames Research Center under the T³ program directed by Dr. Michael Rogers.

References

- [1] E. Masi, J. Bellan, K. G. Harstad, and N. A. Okong'o, Multi-species turbulent mixing under supercritical-pressure conditions: modelling, direct numerical simulation and analysis revealing species spinodal decomposition, *Journal of Fluid Mechanics* 721 (2013) 578–626.
- [2] B. Chehroudi, D. Talley, and E. Coy, Visual characteristics and initial growth rates of round cryogenic jets at subcritical and supercritical pressures, *Physics of Fluids* 14 (2002) 850–861.
- [3] A. Roy, C. Joly, and C. Segal, Disintegrating supercritical jets in a subcritical environment, *Journal of Fluid Mechanics* 717 (2013) 193–202.
- [4] C. Muthukumar and A. Vaidyanathan, Mixing nature of supercritical jet in subcritical and supercritical conditions, *Journal of Propulsion and Power* 33 (2016) 842–857.
- [5] P. J. Morris, Viscous stability of compressible axisymmetric jets, *AIAA Journal* 21 (1983) 481–482.
- [6] A. Michalke, Survey on jet instability theory, *Progress in Aerospace Sciences* 21 (1984) 159–199.
- [7] N. Panchapakesan and J. Lumley, Turbulence measurements in axisymmetric jets of air and helium. Part 1. Air jet, *Journal of Fluid Mechanics* 246 (1993) 197–223.
- [8] H. J. Hussein, S. P. Capp, and W. K. George, Velocity measurements in a high-Reynolds-number, momentum-conserving, axisymmetric, turbulent jet, *Journal of Fluid Mechanics* 258 (1994) 31–75.
- [9] B. Boersma, G. Brethouwer, and F. Nieuwstadt, A numerical investigation on the effect of the inflow conditions on the self-similar region of a round jet, *Physics of fluids* 10 (1998) 899–909.

Sub Topic: Other

- [10] C. Bogey and C. Bailly, Effects of inflow conditions and forcing on subsonic jet flows and noise. *AIAA journal* 43 (2005) 1000–1007.
- [11] W. K. George, The self-preservation of turbulent flows and its relation to initial conditions and coherent structures, *Advances in turbulence* 3973 (1989).
- [12] N. Okong'o, K. Harstad, and J. Bellan, Direct numerical simulations of O₂/H₂ temporal mixing layers under supercritical conditions, *AIAA journal* 40 (2002) 914–926.
- [13] K. G. Harstad, R. S. Miller, and J. Bellan, Efficient high-pressure state equations, *AIChE journal* 43 (1997) 1605–1610.
- [14] L. Sciacovelli and J. Bellan, The influence of the chemical composition representation according to the number of species during mixing in high-pressure turbulent flows, *Journal of Fluid Mechanics* 863 (2019) 293–340.
- [15] B. E. Poling, J. M. Prausnitz, J. P. O'connell, et al., *The properties of gases and liquids*, vol. 5, McGraw-hill New York, 2001.
- [16] E. W. Lemmon, M. L. Huber, M. O. McLinden, et al., NIST standard reference database 23, NIST reference fluid thermodynamic and transport properties—REFPROP, Version 9 (2010) 55.
- [17] D. J. Bodony, Analysis of sponge zones for computational fluid mechanics, *Journal of Computational Physics* 212 (2006) 681–702.
- [18] T. J. Poinsot and S. Lele, Boundary conditions for direct simulations of compressible viscous flows, *Journal of computational physics* 101 (1992) 104–129.
- [19] G. Lodato, P. Domingo, and L. Vervisch, Three-dimensional boundary conditions for direct and large-eddy simulation of compressible viscous flows, *Journal of Computational Physics* 227 (2008) 5105–5143.
- [20] B. J. Boersma, Numerical simulation of the noise generated by a low Mach number, low Reynolds number jet, *Fluid dynamics research* 35 (2004) 425.
- [21] N. Sharan and J. R. Bellan, Numerical aspects for physically accurate Direct Numerical Simulations of turbulent jets, *AIAA Scitech 2019 Forum* (2019), p. 2011.
- [22] N. Sharan, Time-stable high-order finite difference methods for overset grids, PhD thesis, University of Illinois at Urbana-Champaign, 2016.
- [23] N. Sharan, C. Pantano, and D. J. Bodony, Time-stable overset grid method for hyperbolic problems using summation-by-parts operators, *Journal of Computational Physics* 361 (2018) 199–230.
- [24] C. Lubbers, G. Brethouwer, and B. Boersma, Simulation of the mixing of a passive scalar in a round turbulent jet, *Fluid Dynamics Research* 28 (2001) 189.
- [25] S. C. Crow and F. Champagne, Orderly structure in jet turbulence, *Journal of Fluid Mechanics* 48 (1971) 547–591.
- [26] J. Mi, D. Nobes, and G. Nathan, Influence of jet exit conditions on the passive scalar field of an axisymmetric free jet, *Journal of Fluid Mechanics* 432 (2001) 91–125.